Automated Design Optimization of a Three-Dimensional S-Shaped Subsonic Diffuser

Sophia Lefantzi* and Doyle D. Knight[†]
Rutgers University, Piscataway, New Jersey 08854-8058

An automated design optimization process for subsonic S-shaped diffusers was developed and validated. The test case for the process was the evolution of an optimal design for an S-shaped subsonic diffuser, where optimality was based on the minimization of the total pressure distortion at the diffuser exit, while sustaining total pressure recovery. Constraints placed by airframe weight, space, and line-of-sight blockage of the engine face cause subsonic diffusers to be highly divergent and curved, characteristics that lead to strong secondary flows, boundary-layer separation, and inhomogeneity of the total pressure profile. As a part of the design process, we introduce a surface perturbation (bump) on a baseline S-shaped diffuser, and minimize an objective function, reflecting the total-pressure distortion, with respect to the perturbation height and width. To synthesize the automated analysis and optimization method, we created a Subsonic Diffuser Design System (SDDS), which utilizes four commercial/third-party software tools. These tools are Pro/Engineer (a three-dimensional solid modeler for the generation of diffuser geometries), GridPro (an elliptic mesh generator), GASPex (an aerodynamic simulation package), and CFSQP (a gradient-based optimizer to traverse the design space automatically). The integration of Pro/Engineer significantly expands the capability of SDDS to enable multidisciplinary design, for example, include structural and thermal analysis, into the automated design process. Results indicate the development of the surface perturbation and a consequent decrease in total pressure distortion during the convergence to the optimal geometry. We emphasized on the flowfield visualization of the optimal diffuser and detected a complex three-dimensional separation region inside the bump.

Nomenclature

c_p	=	static pressure coefficient
$DC(\psi)$	=	distortion index
d	=	inflow diameter
p	=	static pressure
p_0	=	total pressure
$p_{0,\text{ref}}$	=	total pressure in the core, at the diffuser's entrance
$p_0/p_{0,\text{ref}}$	=	total pressure recovery
q	=	dynamic pressure
R	=	curvature radius of baseline duct, 1.021 m
r_1	=	inlet radius of baseline duct, 0.1021 m
r_2	=	outlet radius of baseline duct, 0.1257 m
θ	=	angle measured along the length
ϕ	=	initiation polar angle of region for DC
ψ	=	angular width of region for DC

Subscript

cl	=	centerline

I. Introduction

A DIFFUSER is a component utilized to decelerate a flow before its entrance in a compressor. To reduce infrared and radar signatures, diffusers are often humped/curved to achieve a line-of-sight blockage of the engine face. This must be done with minimal total pressure losses and flow distortions. High total pressure losses deteriorate propulsion efficiency, and nonuniform flow conditions at the engine face restrict the engine's surge and stall limits. However, airframe weight and space considerations demand the diffuser be as short as possible, which results in a high degree of centerline curvature and large changes in the cross-sectional area. High curvature and large cross-sectional variations result in the development of strong secondary flows and boundary-layer separation, which increase the total pressure nonuniformity and total pressure losses at the exit of the diffuser.

The goal of our research was the creation of a sophisticated subsonic diffuser design method, utilizing state-of-the-art existing commercial and third-party software, and its validation through automated optimal design of an S-shaped subsonic diffuser. We integrated a solid geometric modeler (Pro/Engineer),[1] an elliptic mesh generator (GridPro),[2] an aerodynamic solver (GASPex),[3] and a gradient-based optimizer (CFSQP)[4] in a closed automated design optimization loop. Our design tool was then successfully tested for an S-shaped subsonic diffuser, on which we introduced a surface perturbation with the aim of reducing the total pressure distortion at the exit of the diffuser.

Computations were performed for the baseline S-shaped subsonic diffuser with two different grid sizes. Results exhibited good agreement with existing computational and experimental data. A design optimization process was performed with our automated design tool, resulting in a diffuser with a surface perturbation, which significantly reduced flow distortion at the exit.

For the S-shaped ducts, different experimental studies have been conducted in the incompressible range. In these studies, vortex pairs were formed within the S-shaped ducts due to secondary flows induced by pressure gradients. These counter-rotating vortices are responsible for a low total pressure, low velocity region at the exit plane of the duct. Bansod and Bradshaw[5] found that the pair of the counter-rotating vortices was embedded in the lower part at the exit and expelled low-velocity fluid from the boundary layer toward the center of the exit cross section.

For the compressible range of experiments for S-shaped ducts, the most comprehensive existing benchmark data set is the one obtained by Wellborn et al.[6] The S-shaped diffuser utilized is shown

*Graduate Research Assistant, Department of Mechanical and Aerospace Engineering, 98 Brett Road; currently L.T.E., Reacting Flow Research, P.O. Box 969, Mail Stop 9051, Sandia National Laboratories, Livermore, CA 94551. AIAA Member.

[†]Professor, Department of Mechanical and Aerospace Engineering, 98 Brett Road. Associate Fellow AIAA.
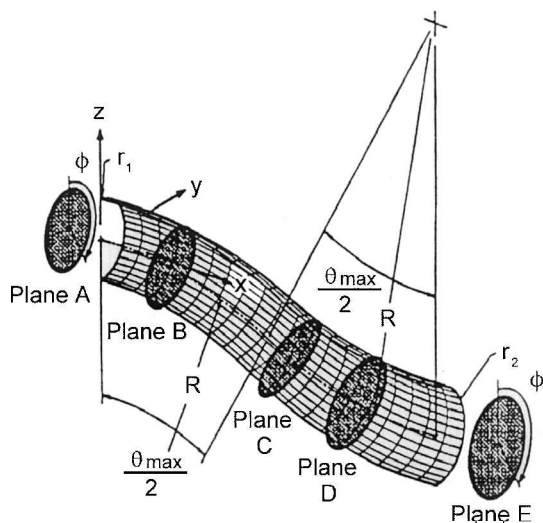
Fig. 1   Baseline S-shaped subsonic diffuser.[6]

in Fig. 1. The results indicated flow symmetry about the $y = 0$ (centerline) plane and strong interaction between the boundary layer and the core flow. A large region of streamwise flow separation was observed within the duct, and strong pressure driven secondary flows were identified, which finally evolved into a pair of counter-rotating vortices. These vortices convected low-momentum fluid from the boundary layer toward the cross-sectional center, thus distorting the uniformity of the total pressure and reducing the magnitude of the total pressure recovery at the exit plane.

Smith et al.[7] studied the performance characteristics of a diffusing subsonic S-duct. They solved the three-dimensional Reynolds averaged Navier–Stokes equations, by using a two-zone (H and O) grid and employing an algebraic turbulence model. Their results indicated good agreement with experimental data, and they concluded that further grid refinement and utilization of a two-equation turbulence model would improve the results. Harloff et al.[8] studied the compressible flow within an S-duct by implementing both the Baldwin–Lomax[9] and the k–ϵ turbulence models. They compared their data to that of Wellborn's et al.[6] and concluded that although the agreement with the experiment was good, both turbulence models underpredicted the length and angular extent of the boundary-layer separation. Zhang[10] performed computational analysis of the S-shaped subsonic diffuser studied by Wellborn et al.[6] by utilizing a two-zone (H and O) grid and the Baldwin–Lomax turbulence algebraic model,[9] to solve the three-dimensional Reynolds averaged Navier–Stokes equations. Zhang[10] obtained good agreement with the Wellborn et al.[6] experimental data, but the turbulence model underestimated the size of the separation. Zhang et al.[11] performed computational analysis with a finer grid and obtained better agreement with the experimental data.

The presence of the two counter-rotating vortices at the exit of the S-shaped subsonic diffuser distorts the flow uniformity. It is desirable to deliver the most uniform flow possible at the engine face to improve the engine performance, for example, to avoid leading-edge shocks at the compressor blades. Designers have used many ways to reduce that distortion. A very important method to eliminate boundary-layer separation is related to vortex generators. Reichert and Wendt[12] studied various configurations of low-profile vortex generator arrays to control the flow in a S-duct. Their research demonstrated that each tested vortex generator array improved the total pressure recovery and that the maximum total pressure distortion drop was obtained by the configuration employing the largest vortex generators. Zhang introduced a Gaussian bump on the S-shaped diffuser's surface and performed a trade optimization study[10] with three design parameters, namely, the streamwise position of the bump, the height of the bump, and the streamwise width of the bump. Zhang's research demonstrated that the introduction of the bump on the surface of the diffuser significantly reduces the total pressure distortion at the exit plane, typically up to 70%. She also demon-

strated that the total pressure distortion is reduced as the height and the width of the bump are increased and that the optimal streamwise placement of the bump is before the region at which the flow separation occurs.

II.   Objective

The objectives of our research are twofold. The first objective is the development of a Subsonic Diffuser Design System (SDDS), which utilizes commercial/third-party software wherever possible to obtain the optimal aerodynamic design of a S-duct subsonic diffuser. The SDDS is written in Perl. SDDS controls the execution of the codes for computer-aided design (Pro/Engineer),[1] grid generation (GridPro),[2] flow simulation (GASPex)[3] and optimization (CFSQP)[4] in the proper sequence and on the appropriate computer systems within the network and manages the interaction between the codes. The second objective is improved physical understanding of the effect of a surface bump on the flow distortion at the outflow of an S-duct diffuser. Particular emphasis is placed on flowfield visualization of the complex three-dimensional separation generated by the surface bump.

This research represents an important extension of the previous results by Zhang[10] and Zhang et al.[11] with regard to both objectives. SDDS utilizes the Pro/Engineer[1] CAD software (although, in principle, another CAD software system could also be used), whereas Zhang[10] developed a specific geometric model for the S-duct diffuser using Non-Uniform Rational B-Splines (NURBS). The integration of a sophistical CAD system such as Pro/Engineer significantly expands the capability of the SDDS to enable multidisciplinary design, for example, structures, into the automated design process. Typically, CAD systems are utilized in a stand-alone manner in the industry, with users transferring information between CAD and other programs manually. The demonstration of the capability to automate fully the integration of a commercial CAD system into a design optimization cycle is an important contribution. Also, this research provides substantial new insight into the flowfield structure associated with the surface bump and its effect on the total pressure distortion at the outflow.

III.   Optimization Strategy

The concept of our design process is simple yet very powerful. Our design strategy (Fig. 2), consists of the following steps.

1) We parametrically represent, in Pro/Engineer,[1] the geometry of the subsonic diffuser. Our test case, that is, the S-shaped diffuser, is designed as a single part. We export a surface grid in NASTRAN format.

2) We generate a Navier–Stokes (H and O) grid using GridPro.[2]

3) We compute the aerodynamic flowfield with GASPex.[3]

4) We compute the objective function of our optimization, that is, the total pressure distortion index at the exit of the diffuser, with our f77 code utilizing Triangle[13] to generate a two-dimensional mesh on the circular exit area.

5) We modify the diffuser's design parameters using CFSQP.[4] Step 5 provides the new values of the design parameters, which in turn are fed back to Pro/Engineer[1] and generate a new geometry for the diffuser. Steps 1–5 are iterated until the optimal diffuser design is achieved.
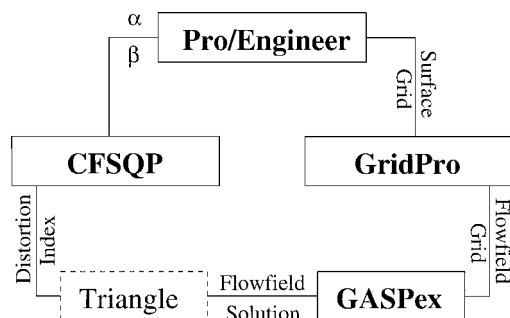

Fig. 2   Design strategy.

IV. Test Case

To ensure that the aerodynamic problem was properly defined, we chose a test case, for which experimental and computational data were available, that is, the baseline S-shaped subsonic diffuser. We performed two computations with GASPex[3] for the baseline diffuser and compared our results with the experimental results of Wellborn et al.[6] and the computations of Zhang,[10] Zhang et al.,[11] and Harloff et al.[8]

The measure of merit we used for our study is the total pressure distortion index described over the two-dimensional circular domain at the exit of the diffuser (Fig. 3). The total pressure distortion index is defined as:

$$DC(\psi) = \max_{0 < \phi \le 2\pi} \left[\frac{\bar{p}_0 - \bar{p}_0(\phi, \psi)}{\bar{q}} \right] \qquad (1)$$

where ϕ is the starting angle for a pie segment of angle ψ of the diffuser exit. It is

$$\bar{p}_0 = \frac{\int_0^{2\pi} \int_0^R p_0(r, \theta) r \, dr \, d\theta}{\int_A dA}$$

$$\bar{p}_0(\phi, \psi) = \frac{\int_0^{\psi} \int_0^R p_0(r, \phi + \theta) r \, dr \, d\theta}{\int_A dA}$$

$$\bar{q} = \frac{\int_A q \, dA}{\int_A dA}$$

The evaluation of the total pressure distortion index requires, first, calculation of an area integral over a circular segment of angle ψ. A segment is described by its starting point ϕ and its segment angle, for example, $\psi = 45$ deg. Second, the index requires calculation of the distortion index for a variety of positions of this 45-deg segment, so that we can finally choose the maximum distortion for the given total pressure field.

Our method of calculating the total pressure distortion index was successfully tested for the case of an analytic function.

A. Baseline Computation Results

To verify the proper utilization of the computational fluid dynamics solver, GASPex,[3] we performed simulations for the baseline S-shaped subsonic diffuser (Fig. 1). This configuration is the same as used by Wellborn et al.[6] for their experiments. For our Reynolds averaged Navier–Stokes computation, the inflow Mach number at the centerline was 0.6, and the inlet Reynolds number based on the

inlet diameter was 2.6×10^6. The inlet boundary-layer thickness was 7.3% of the inlet diameter. The modified Baldwin–Lomax turbulence model was utilized. We made use of the symmetry about the $y = 0$ plane, thus only half of the baseline configuration was used during the computation. Two computations were performed with different grid sizes:

1) The first computation had a two-zone Navier–Stokes grid, that is, H grid ($9 \times 13 \times 133$) and O grid ($29 \times 73 \times 133$), resulting in a total of 297,122 grid points. Hereafter, this computation will be addressed as the coarse grid computation.

2) The second computation had a two-zone Navier–Stokes grid, that is, H grid ($17 \times 25 \times 265$) and O grid ($57 \times 145 \times 265$), resulting in a total of 2,302,850 grid points. Hereafter, this computation will be addressed as the fine grid computation.

Our results are compared with the experiments of Wellborn et al.[6] and the computations of Zhang,[10] Zhang et al.,[11] and Harloff et al.[8] The grids utilized for our computations, the Zhang[10] and Zhang et al.[11] computations, and the Harloff et al.[8] computation are listed in Table 1. For the Harloff et al. grid distributions, all grid densities for the O grids are listed for the radial, circumferential, and axial directions, respectively.

The total pressure distortion at the exit plane E (Fig. 1) is evident for both the coarse and the fine grid computations (Figs. 4a and 4b, respectively). For the coarse grid computation, we plotted some of the streamlines near the diffuser's surface, and we can trace a region of separation (Fig. 5a) at the lower part of the diffuser before the first bend. That separation region becomes clear with the fine grid computation (Fig. 5b).

By comparing the distortion indices values obtained for different pie segments ψ at the exit plane E, with the values obtained
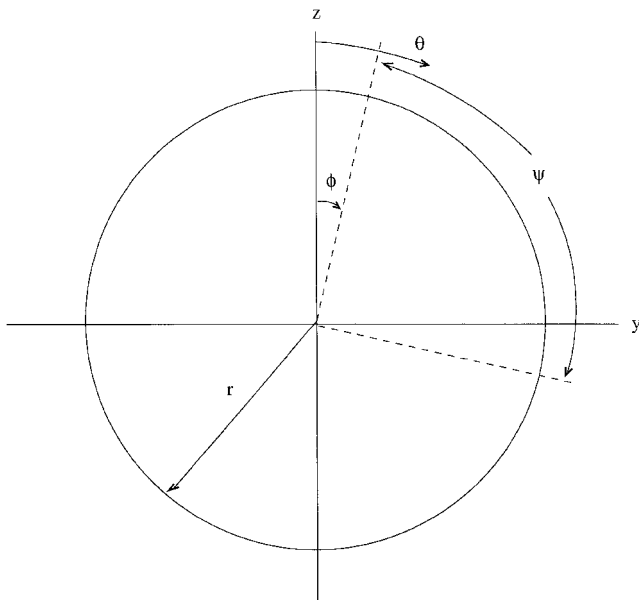
a)

b)
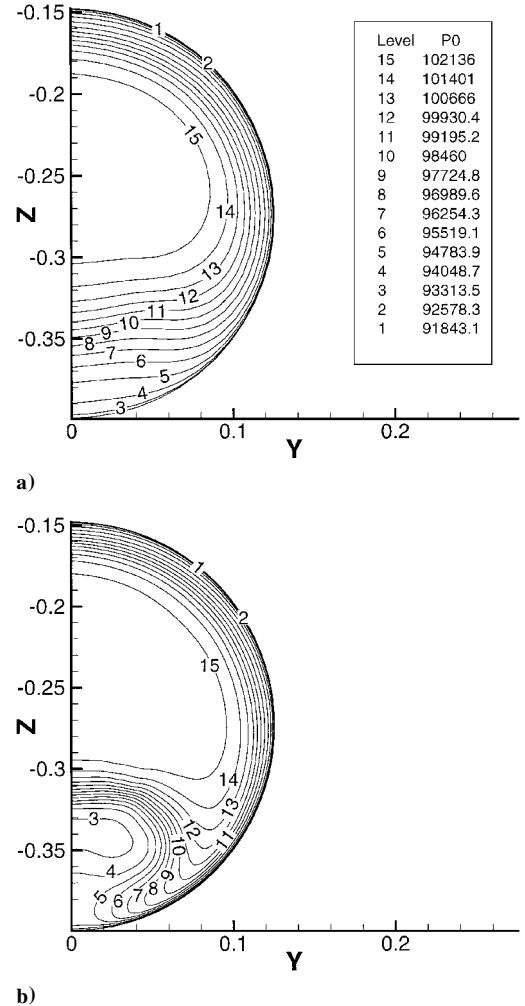
Fig. 4 Total pressure contours at plane E for a) coarse grid and b) fine grid.

Fig. 3 Two-dimensional circular domain at the exit of the diffuser.

Table 1   Grid densities

Method	H grid	O grid	O grid 1	O grid 2	O grid 3
Computation, coarse grid	$9 \times 13 \times 133$	$29 \times 73 \times 133$	——	——	——
Computation, fine grid	$17 \times 25 \times 265$	$57 \times 145 \times 265$	——	——	——
Zhang,[10] coarse grid	$9 \times 13 \times 133$	$29 \times 73 \times 133$	——	——	——
Zhang et al.,[11] fine grid	$17 \times 25 \times 265$	$57 \times 145 \times 265$	——	——	——
Harloff et al.,[8] grid	$11 \times 15 \times 129$	——	$53 \times 71 \times 32$	$53 \times 71 \times 69$	$53 \times 71 \times 32$

Table 2   Distortion index comparison

Method	DC, 45 deg	DC, 90 deg
Experiment	0.5590	0.3700
Computation, coarse grid	0.3454	0.3046
Computation, fine grid	0.5968	0.4827
Zhang,[10] coarse grid	0.4422	0.3752
Zhang et al.,[11] fine grid	0.7000	0.6220
Error, coarse grids, %	−21.89	−18.81
Error, fine grids, %	−14.74	−22.39

a)

b)
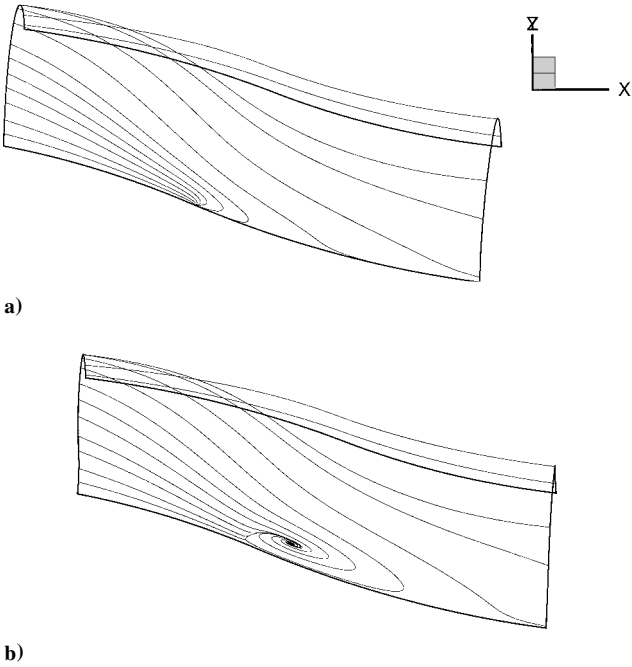
Fig. 5   Baseline surface flow separation for a) coarse grid and b) fine grid.

Fig. 6   Surface static pressure coefficient at $\phi = 10$ deg: ———, coarse grid computation; - - - -, fine grid computation; –··–, Zhang[10] coarse grid; – – –, Zhang et al.[11] fine grid; ·····, Harloff et al.,[8] and □, experiment.

Fig. 7   Surface static pressure coefficient at $\phi = 90$ deg: ———, coarse grid computation; - - - -, fine grid computation; –··–, Zhang[10] coarse grid; – – –, Zhang et al.[11] fine grid; ·····, Harloff et al.,[8] and □, experiment.

by Wellborn et al.,[6] Zhang[10] and Zhang et al.[11] (Table 2), we can conclude that our coarse grid computation underpredicts the distortion level at the diffuser's exit plane, whereas our fine grid computation slightly overpredicts it when comparing with the experiment. In Table 2, the error between our computations and the Zhang[10] and Zhang et al.[11] computations is shown. The total pressure distortion is influenced by the the separation prediction at the lower part of the diffuser and by the strong pressure driven secondary flows developed within the diffuser flowfield. Our fine grid computation distortion index has better agreement with the measurements, and a logical explanation for this is that our computation predicts more accurately the development and behavior of the two counter-rotating vortices. The method and definitions used for our fine grid computation and the Zhang et al.[11] fine grid computation are practically the same, but the discrepancy of the results can be attributed to that the grids were not identical and that the region searched for the maximum in the outer function of the Baldwin–Lomax model was different in the computation of Zhang et al.[11] compared to the present case.

Some of the computed results for the baseline S-shaped diffuser are presented in Figs. 6–8, displaying the static pressure coeffi-
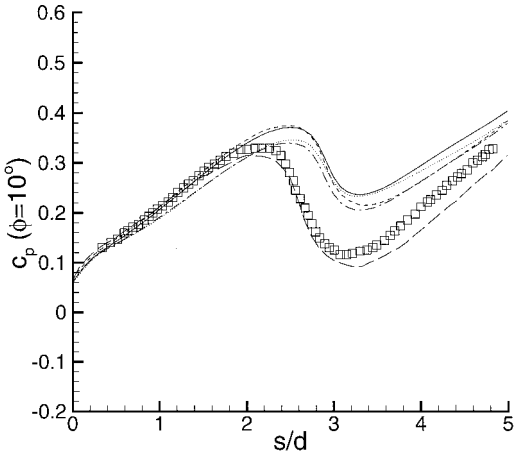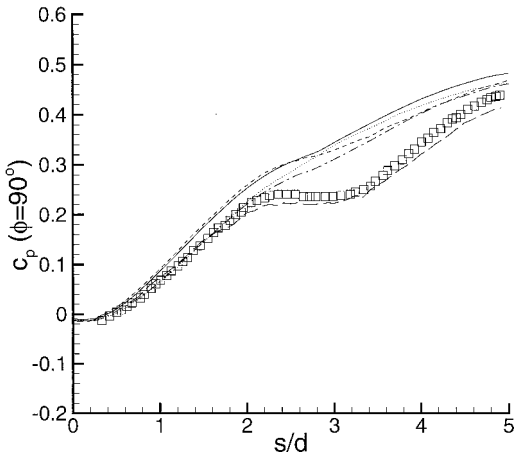
cient c_p at three circumferential locations ($\phi = 10, 90$, and 170 deg), where ϕ is the cross-stream polar angle defined in Fig. 1. Our computed results are presented along with the experimental results obtained by Wellborn et al.[6] and the sets of computational results obtained by Zhang[10] and Zhang et al.[11] and Harloff et al.[8] The Baldwin–Lomax algebraic turbulence model[9] was used for all of the computational results presented. The static pressure coefficient is defined as

$$c_p = \frac{p - p_{cl}}{p_{0,cl} - p_{cl}} \qquad (2)$$

where p is the local static pressure and $p_{0,cl}$ and p_{cl} are the total and static pressure at the inflow centerline, respectively. The computations and the experiment agree as long as the flow is attached. Around $s/d \approx 2.0$, c_p undergoes a significant decrease at all three circumferential locations due to boundary-layer separation.
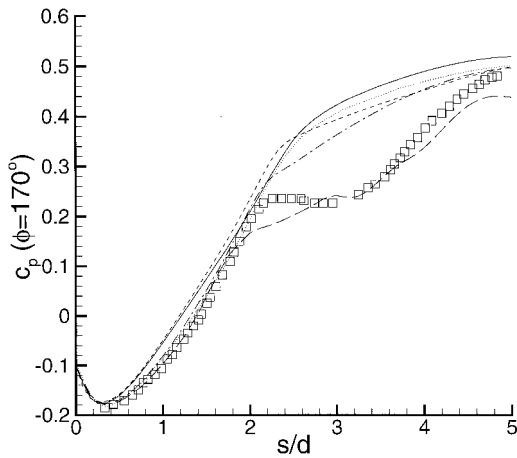
Fig. 8   Surface static pressure coefficient at $\phi = 170$ deg: ———, coarse grid computation; - - - -, fine grid computation; –·–, Zhang[10] coarse grid; – – –, Zhang et al.[11] fine grid; ·····, Harloff et al.,[8] and □, experiment.

In Fig. 6, we capture the separation location, but it is overpredicted ($s/d \approx 2.5$ as opposed to ≈ 2.0 in the experimental results). The turbulence model, characteristically, fails to capture it except for the fine grid calculation of Zhang et al.,[11] where the region searched for the maximum in the outer function evidently changed the magnitude of the eddy viscosity to a sufficient extent to achieve an accurate prediction of the separation location and better agreement with the surface pressure measurements. The principal difference between our fine grid computation and the Zhang et al.[11] fine grid computation is the tuning of the Baldwin–Lomax turbulence model Zhang et al.[11] implemented, which resulted in better agreement with the surface pressure measurements.

Our baseline results indicate that our calculations have relatively good agreement with the existing experimental and computational data. Figures 6–8 indicate that we obtained very close agreement with the Harloff et al.[8] computational results for both our coarse and fine grid simulations. Harloff et al. used the Baldwin–Lomax turbulence model as well, but their grid dimensions[8] were different than ours. Our computations predict the major characteristics of the flowfield, namely, the flow separation at the lower part of the diffuser and the total pressure distortion at the exit of the diffuser.

V.   Optimization

We optimize the shape of the perturbed S-shaped subsonic diffuser with two design parameters and a single-valued objective function, using a gradient-based optimization algorithm. In general, when the design domain is smooth (which is our case) and the derivatives are continuous, gradient-based algorithms converge faster than nongradient algorithms. Trade studies we conducted using a single design variable showed a smooth variation of the objective function with changes in the design variable. Moreover, the gradient-based optimizer exhibited no tendency to become trapped in local minima. It would have been interesting to include more design parameters in our optimization process, for example, the streamwise position and the cross-sectional base opening of the bump. However, Zhang's trade study[10] indicated that the optimal streamwise placement of the bump is immediately upstream the separation location on the lower portion of the diffuser, and single aerodynamic simulations we performed indicated that increasing the cross-sectional opening of the bump deteriorates the total pressure uniformity at the exit, whereas decreasing it further results in a slotlike bump. Thus, to save computational time, two design parameters were included in the optimization process.

The two design parameters used are the height α and the streamwise width β of the bump. The design constraints are $0.1257 \leq \alpha \leq 0.8$ m and $0.2 \leq \beta \leq 0.6$ m. The choice of the lower and upper bound for each design parameter was made in a way that limits the shape modification within a physically realizable region.
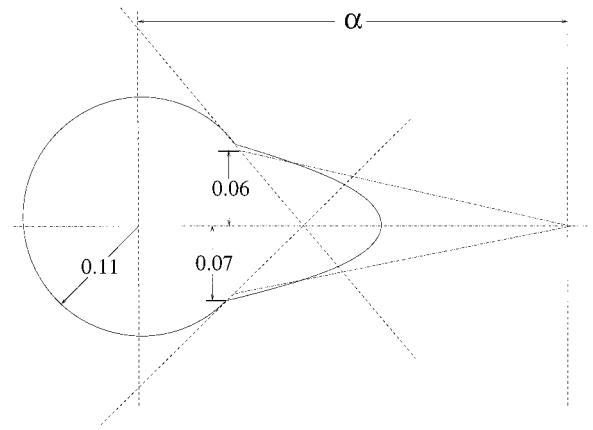
Fig. 9   Cross section perturbed with a spline.

The maximum base opening of the bump, cross sectionally, is 63% of the corresponding diameter (Fig. 9). The objective function is the total pressure distortion index at the diffuser's exit (1). The distortion index is evaluated for a pie segment of $\psi = 45$ deg. According to the trade study performed by Zhang,[10] the evaluated distortion index for different angles of the pie segment, when the bump size changes, exhibits similar behavior as that of a 45-deg segment. Optimization runs were performed for different step and bound values of the design constraints, using coarse grids.

A.   Grid Sensitivity

Our two design optimization constraints are the height and the width of the bump, so we had to make sure that the resulted grid for the bump region was properly achieved. After carefully reviewing the generated grid for each iteration, we observed that as the bump gets higher and wider the grid on the tip of the bump (Fig. 10a) can become very skewed, and we cannot trust the flow solution resulting from such a grid. To solve the problem, we modified the automated grid generation files to detect the position of the bump and to apply a forced high grid resolution in the bump region lengthwise. The updated grid at the bump neighborhood for one of the iterations is presented in Fig. 10b.

B.   Optimization Results

Once we obtained an acceptable automated grid generation for all of the iterations, we performed the final optimization run. The run was performed with the coarse grid distribution, to save computational time. The resulted improvement of the total pressure distortion index, for all of the optimization iterations, is presented in Table 3. The coarse grid baseline total pressure distortion index value is 0.3454, for a pie segment of 45 deg, and the improvement estimation is based on that value. The total pressure recovery at exit plane E of the diffuser is also presented in Table 3. We can see that the total pressure recovery remains essentially the same. Hence, the bump introduction did not increase the total pressure losses, compared to the baseline S-shaped diffuser, which agrees with the Zhang et al. results.[11] One would expect that the mixing within the bump would reduce the total pressure recovery at the exit. However, the total pressure recovery also depends on the secondary flow (counter-rotating vortices) development. When the secondary flow development is reduced through the introduction of the bump, the total pressure recovery tends to increase. Thus, the introduction of the bump has two opposite effects, and the net result has no significant change.

The optimizer converged after seven iterations. Each complete iteration needs approximately 22 h on a single processor R10000 SGI, and we observed that the optimizer consistently tends to increase the height and the width of the bump. This agrees with Zhang's[10] observation.

The optimized diffuser shape is shown in Fig. 11. If we compare the total pressure contours at exit plane E (Fig. 12a) for the optimal diffuser, with the total pressure contours at exit plane E for the

Table 3   Distortion index, distortion index improvement, total pressure recovery, and total pressure recovery relative deviation vs iterations

Iteration	DC 45 deg	Improvement, %	$p_0/p_{0,\text{ref}}$	$p_0/p_{0,\text{ref}}$ relative deviation, %
1	0.3365	2.576	0.9680	0.259
2	0.3198	7.412	0.9671	0.166
3	0.3338	3.358	0.9686	0.321
4	0.1599	53.7	0.9650	−0.052
5	0.07	79.7	0.9641	−0.145
6	0.0639	81.5	0.9645	−0.072
7	0.0638	81.5	0.9644	−0.114
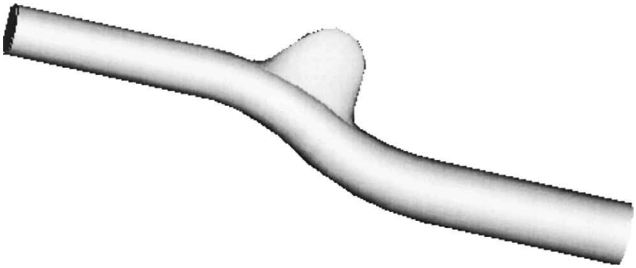
Fig. 11   Optimized diffuser.
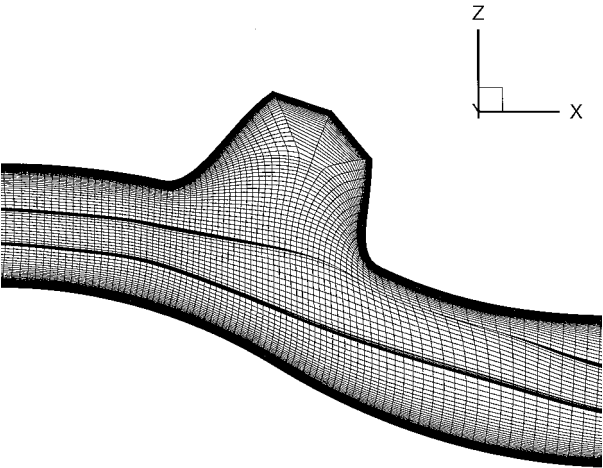
Fig. 10a   Grid nonuniformity.

Fig. 10b   Updated grid.

a)

b)

Fig. 12   Total pressure contours, at the exit plane E, optimal diffuser for a) coarse grid and b) fine grid.
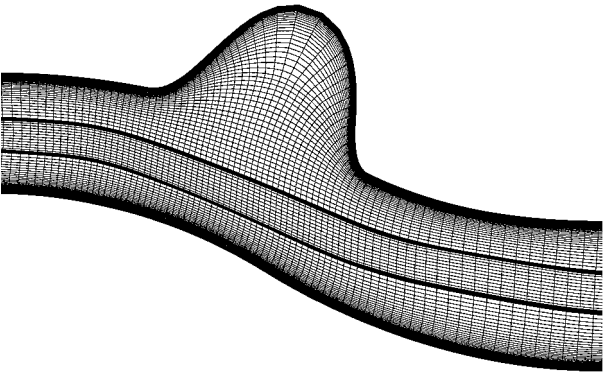
baseline S-shaped diffuser (Fig. 4a), we can see that the total pressure distortion is significantly reduced. We can attribute that reduction to the introduction of the bump, which creates a separation region inside the bump (Fig. 13a). For the optimized diffuser, the cross-sectional swirl at the exit plane E (Ref. 14) has been redirected in a way that makes the low-momentum fluid distribute more uniformly.

Our optimization process for the S-shaped subsonic diffuser proved the design optimization loop works reliably and provides an optimal solution. The optimizer resulted in a diffuser with an estimated total pressure distortion approximately 81% less than that of the baseline S-shaped diffuser.

To verify that our fast optimization process for which the coarse grid was used indeed results in an optimized design, we considered the optimal diffuser's shape and performed a single run with GASPex[3] utilizing the fine grid distribution. The total pressure contours at exit plane E (Fig. 12b) for this run indicate significantly reduced distortion, compared to the baseline fine grid run (Fig. 4b). The resulting total pressure distortion index for the optimal diffuser is $DC(45 \text{ deg}) = 0.3759$. If we compare this result with the fine grid
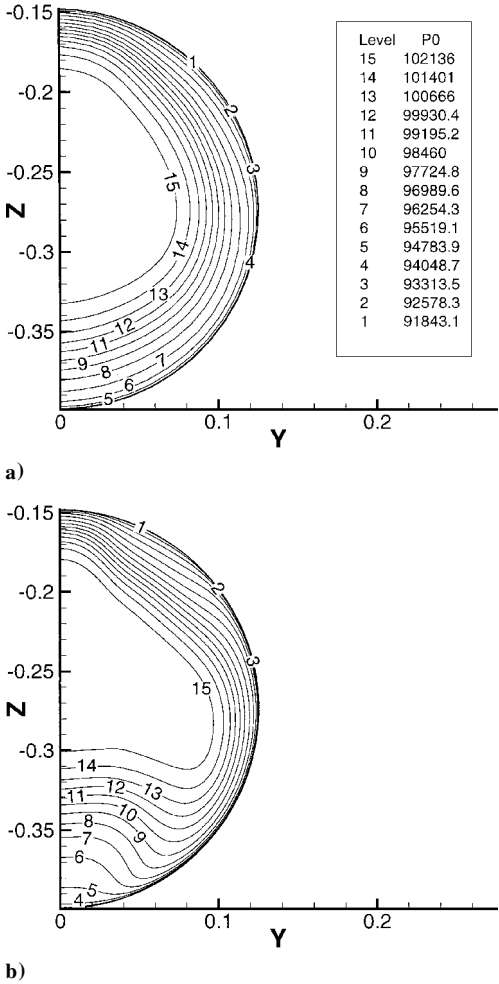
baseline total pressure distortion index, which was 0.5968, we conclude that indeed the optimized diffuser's shape results in a smaller total pressure distortion, improved by 37%. This improvement is smaller than the one indicated with the coarse grid optimization run. This can be attributed to the stretching of the grid when the bump was introduced, thus forcing the coarse grid to underresolve the bump region. With the fine grid, the separation region inside the bump is also detected (Fig. 13b), and the cross-sectional swirl at the exit plane E is also significantly reduced compared to that of the baseline fine grid run.

Overall, we can say that both the coarse and the fine grid runs for the optimal diffuser's shape qualitatively predict the same flow behavior and that their quantitative discrepancies can be attributed to that the coarse grid run was not converged with respect to the grid. The benefit of performing the optimization with the coarse grid lies in that a significantly improved design for the diffuser was obtained in 6.4 days. Although the coarse grid computations were not converged with respect to the grid, the overall design

a)

b)
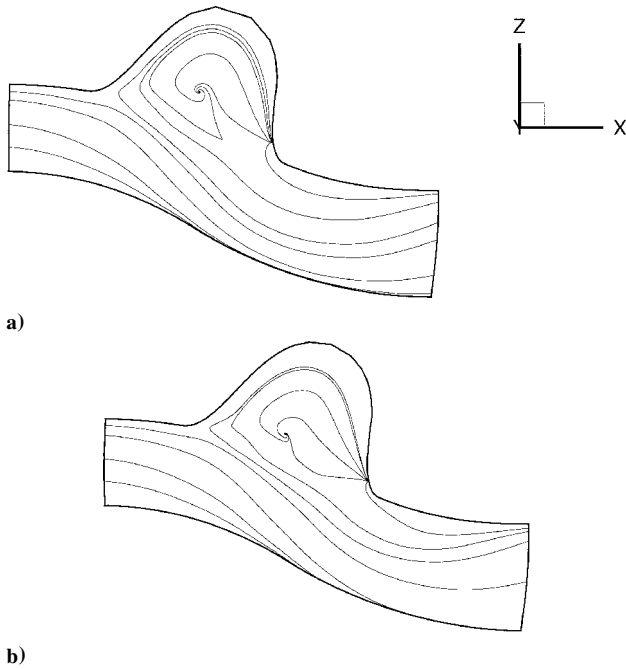
Fig. 13   Streamlines close to the surface for a) optimal coarse grid diffuser and b) optimal fine grid diffuser.

tendency was insensitive to the grid resolution because the flowfield captured the dominant physical phenomena. If the fine grid was utilized for the optimization there would have been a more accurate prediction of the total pressure distortion index and probably a bump with somewhat different size. However, the computational cost would have been excessively large. When it is assumed that the optimizer would once again converge after seven iterations, a single processor run would require seven processor months. The goal of our optimization test was to provide proof of concept and methodology; therefore, the coarse grid optimization test was appropriate.
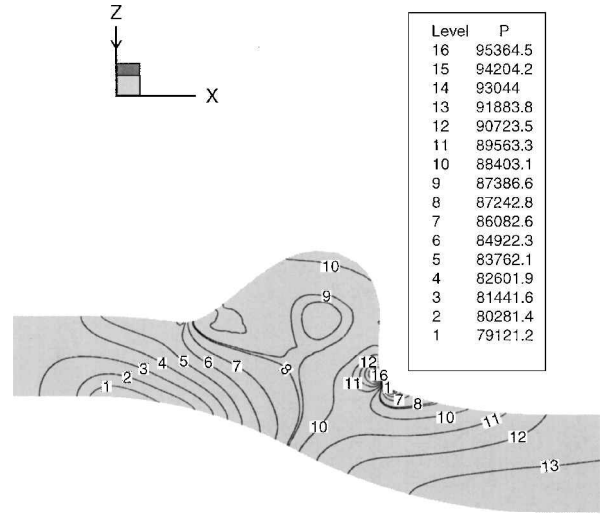
C.   Optimization Results Evaluation

The introduction of a surface perturbation (bump) on the S-shaped subsonic diffuser resulted in a more uniform total pressure distribution at the exit of the diffuser. In Fig. 14a, we plotted the static pressure contours at the plane of symmetry $y = 0$. We can detect a separation region at the end base of the bump lengthwise, indicated by the high static pressure there and verified by the low-velocity magnitude (Fig. 14b) in the neighborhood of the region.

In an effort to better understand the complex three-dimensional separated flowfield associated with the bump, we visualize some of the important volume streamtraces of the flow using Tecplot.[15]

In the baseline diffuser, flow particles entering near the lower surface undergo a three-dimensional rotation as they move downstream due to the secondary flow resulting from the centerline curvature. In Fig. 15, we plotted three volume lines for our fine grid baseline simulation. The flow moves in the direction of the positive x axis, and if the reader reaches out to touch the diffuser, its curved side would be touched. The core flow volume line A smoothly moves along the centerline from the entrance to the exit. Another volume line B originates near the upper part of the surface at the entrance and crosses to the lower part at the exit. The volume line C originating near the lower part of the surface at the entrance undergoes a three-dimensional rotation as it moves downstream. Volume lines behaving like the last one cause a swirling flow region at the lower part of the diffuser.

In Fig. 16a, we plot two volume lines for our coarse grid optimal design simulation. Once again the core flow volume line A moves smoothly. There are volume lines, for example B, originat-
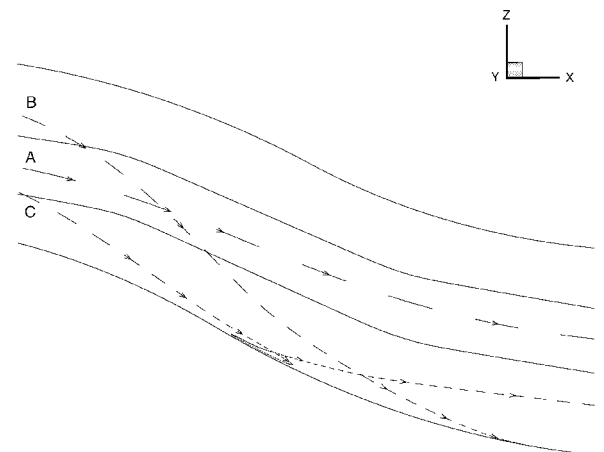

a) Static pressure
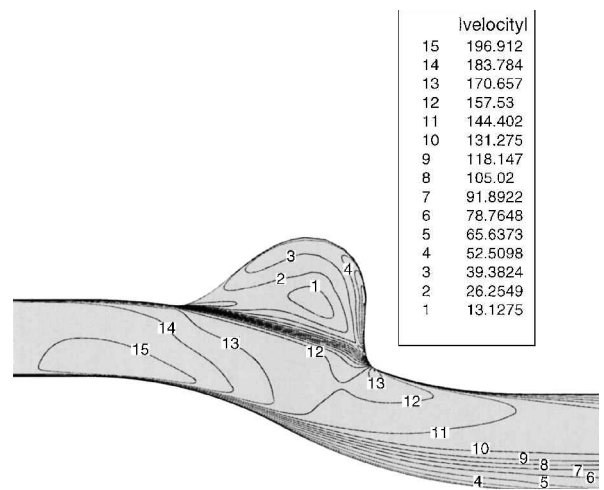
b) Velocity magnitude

Fig. 14   Fine grid, optimal design, at symmetry plane $y = 0$.

Fig. 15   Fine grid, baseline, three-dimensional streamtraces.

ing at the entrance's upper part within the region of the opening of the bump cross sectionally that enter the bump and perform swirling motion within it. We plotted one of these volume lines B in Fig. 16b, where we can see the three-dimensional rotational motion within the bump with larger radius near the $y = 0$ symmetry plane. The fine grid computation verified this flowfield behavior within the bump. In Fig. 17a we can see the rotational motion of the streamtrace in the bump. The volume line enters the bump
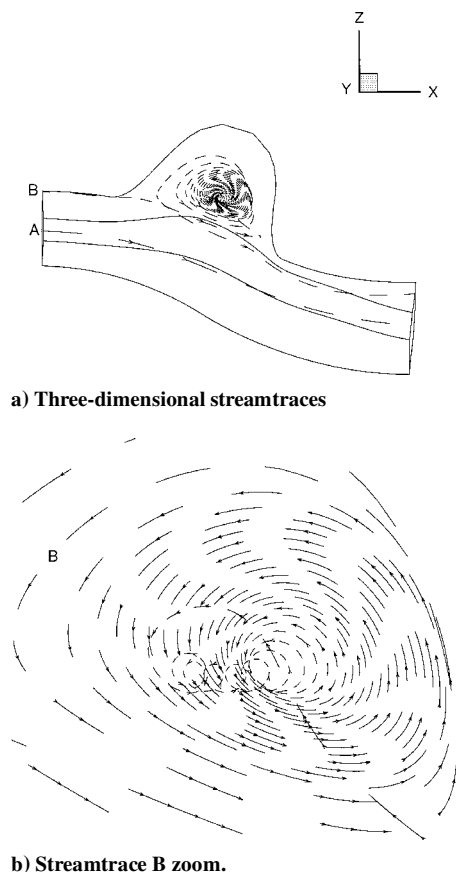
a) Three-dimensional streamtraces

b) Streamtrace B zoom.

Fig. 16   Coarse grid, optimal design.
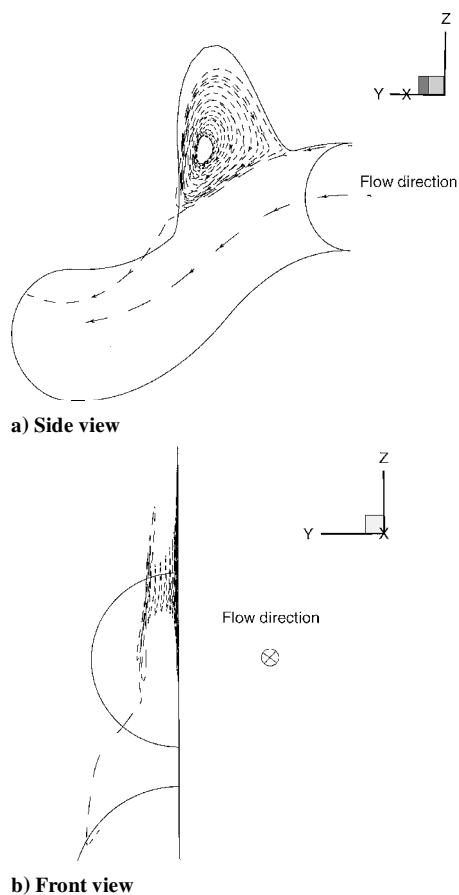

a) Side view

b) Front view

Fig. 17   Fine grid, optimal design, three-dimensional streamtraces.

region near the $y = 0$ symmetry plane, and instead of following the bump curvature and exit, it gets trapped in the rotational flow region and rotates along the y direction toward the bump wall. The front view (Fig. 17b) indicates that the volume line moves in a decreasing radius spiral toward the wall, and as it reaches very close to the wall, its rotational radius increases, and it escapes to the exit of the diffuser.

VI.   Conclusions

Our research study consisted of the integration of four validated commercial/third-party codes (Pro/Engineer,[1] GridPro,[2] GASPex,[3] and CFSQP[4]) in a SDDS utilized for automated design optimization. The integration was achieved with Perl scripts, serving as the links amongst the codes and the different servers that each code was installed on. The interface codes needed for the connection of two consecutive codes were written in FORTRAN 77 and/or C. We evaluated the aerodynamic definition and the solution technique of the flowfield simulation through a test case, that is, the baseline S-shaped subsonic diffuser. The obtained computational results were successfully compared with existing experimental and computational data. We utilized the automated design optimization tool to optimize the S-shaped subsonic diffuser's shape. The optimization goal was the reduction of the total pressure distortion at the exit of the diffuser. The total pressure distortion index (1) was used as the optimization objective function. A bump was introduced on the upper surface of the baseline S-shaped subsonic diffuser ahead of the location for which we traced flow separation with the baseline computation. The bump was designed with two degrees of freedom: its height and its streamwise width. These were our two optimization design parameters.

The results of the research follow:

1) The subsonic diffuser design optimization tool is fully automated. The total pressure distortion index at the diffuser's exit was decreased by 37% according to the fine grid computation we performed for the optimal diffuser's shape that resulted from the coarse grid optimization process. This automated tool can be employed for other design processes as well.

2) Pro/Engineer[1] can be used in an automated process, even though it is primarily intended to serve users interactively.

3) For the aerodynamic computation of the baseline S-shaped subsonic diffuser, we obtained good agreement with the Zhang,[10] Zhang et al.,[11] and Harloff et al.[8] computational data. We predicted the two major field properties, namely, the flow separation at the lower part of the diffuser and the total pressure distortion at the exit of the diffuser. Therefore, we were able to proceed and perform the optimization process.

4) For the optimal diffuser design, we detected a complex three-dimensional separation region inside the bump, and with flowfield visualization we gained valuable physical understanding of its structure.

References

[1]"Pro/Engineer User's Guide," 1996, Parametric Technology Corp., 140 Kendrick Street Needham, MA 02494, USA.

[2]"GridPro/az3000 User's Guide and Reference Manual," 1996, Program Development Corp., 300 Hamilton Ave. Suite 409, White Plains, NY 10601, USA.

[3]General Aerodynamic Simulation Program, Aerosoft, Inc., 1996, 1872 Pratt Drive, Suite 1275, Blacksburg, VA 24060, USA.

[4]Lawrence, C., Zhou, J. L., and Tits, A. L., "User's Guide for CFSQP, A C Code for Solving (Large Scale) Constrained Nonlinear (Minimax) Optimization Problems, Generating Iterates Satisfying All Inequality Constraints," Tech. Rept. TR-94-16rl, The Inst. for Systems Research, Univ. of Maryland, Nov. 1994.

[5]Bansod, P., and Bradshaw, P., "The Flow in S-shaped Ducts," *Aeronautical Quarterly*, Vol. 23, No. 2, 1972, pp. 131–140.

[6]Wellborn, S. R., Reichert, B. A., and Okiishi, T. H., "Experimental Investigation of the Flow in a Diffusing S-Duct," AIAA Paper 92-3622, 1992.

[7]Smith, C. F., Bruns, J. E., Harloff, G. J., and DeBonis, J. R., "Three-Dimensional Compressible Turbulent Computations for a Diffusing S-duct," NASA CR 4392, 1991.

[8]Harloff, G. J., Reichert, B. A., and Wellborn, S. R., "Navier–Stokes Analysis and Experimental Data Comparison of Compressible Flow in a Diffusing S-Duct," AIAA Paper 92-2699, 1992.

[9]Baldwin, B. S., and Lomax, H., "Thin-Layer Approximation and Algebraic Model for Separated Turbulent Flows," AIAA Paper 78-257, 1978.

[10]Zhang, W., "Three Dimensional Subsonic Diffuser Design Optimization and Analysis," Ph.D. Dissertation, Rutgers Univ., Dept. of Mechanical and Aerospace Engineering, Piscataway NJ, May 1999.

[11]Zhang, W., Knight, D., and Smith, D., "Automated Design of a Three-Dimensional Subsonic Diffuser," *Journal of Propulsion and Power*, Vol. 16, No. 6, 2000, pp. 1132–1140.

[12]Reichert, B. A., and Wendt, B. J., "Experimental Investigation of S-Duct Flow Control Using Arrays of Low-Profile Vortex Generators," AIAA Paper 93-0018, 1993.

[13]Shewchuk, J. R., "Triangle: Engineering a 2D Quality Mesh Generator and Delaunay Triangulator," *First Workshop on Applied Computational Geometry*, Philadelphia, Pennsylvania Association for Computing Machinery, May 1996, pp. 124–133.

[14]Lefantzi, S., and Knight, D., "Automated Design Optimization for Subsonic Diffusers," AIAA Paper 2001-3294, 2001.

[15]"Tecplot User's Manual, Version 7.5," 1998, Amtec Engineering, Inc., 13920 SE East-Gate Way Suite 220, Bellevue, WA 98005, USA.